Journal of
Materials Chemistry B

Materials for biology and medicine

Accepted Manuscript

This article can be cited before page numbers have been issued, to do this please use: S. Patra, Z. Papadopoulos, J. Sanz-Villafruela, J. Karges and A. Galstyan, *J. Mater. Chem. B*, 2026, DOI: 10.1039/D6TB00671J.

ROYAL SOCIETY OF CHEMISTRY

rsc.li/materials-b

View Article Online
DOI: 10.1039/D6TB00671J

ARTICLE

Encapsulation of a Ruthenium-Platinum Photosensitizer into Nanofibrous Membranes for Antibacterial Photodynamic Therapy

Santanu Patra,[a#] Zisis Papadopoulos,[b,c#] Juan Sanz-Villafruela,[b,c] Johannes Karges,[b,c*] Anzhela Galstyan [a,d*]

Received 00th January 20xx,
Accepted 00th January 20xx

DOI: 10.1039/x0xx00000x

The global rise of multidrug-resistant microorganisms necessitates antimicrobial technologies that avoid the resistance mechanisms associated with conventional antibiotics and chemical disinfectants. Light-activated antimicrobial systems represent a promising alternative because they generate reactive oxygen species in situ, producing rapid and broad-spectrum pathogen inactivation through non-specific oxidative damage to multiple cellular targets. Such multitarget activity significantly reduces the probability of resistance development. Herein, the chemical synthesis, photophysical and biological evaluation of the encapsulation of a binuclear ruthenium-platinum photosensitizer into electrospun nanofibrous membranes for antimicrobial photodynamic therapy is reported. The binuclear photosensitizer was found to produce singlet oxygen by energy transfer and superoxide through electron transfer, enabling a combined Type I and Type II photochemical mechanisms. The complex was incorporated into electrospun nanofibrous membranes based on polyacrylonitrile and polycaprolactone, yielding high-surface-area materials. Systematic optimization of the fabrication process produced bead-free fibers with controlled morphology, while comparative analysis revealed superior photosensitizer retention and structural stability in the hydrophilic polyacrylonitrile matrix. Under visible-light irradiation, both membrane systems exhibited strong antibacterial activity against Gram-positive and Gram-negative bacteria. The presence of sodium azide increased bacterial inactivation, suggesting that the antimicrobial activity shifted from primarily singlet-oxygen–based damage to a mechanism dominated by radical-mediated oxidative stress. Durability studies under prolonged bacterial exposure demonstrated that membrane performance is governed not only by molecular photochemistry but also by matrix-dependent antifouling resilience. The polyacrylonitrile-based membrane retained structural integrity and antibacterial efficacy after aging, whereas polycaprolactone-based systems showed pronounced fouling and reduced activity. These results establish a direct link between molecular photosensitizer engineering, nanofabrication strategy, and long-term functional performance, providing a blueprint for next-generation photodynamic antimicrobial materials.

Introduction

The rapid global proliferation of multidrug-resistant microorganisms has created an urgent demand for alternative antimicrobial technologies that can overcome the limitations of conventional antibiotics and chemical disinfectants.[1] Traditional antimicrobial agents typically rely on specific biochemical targets, which facilitates the emergence of resistance through genetic adaptation. Consequently, there is increasing interest in antimicrobial strategies that operate through non-specific, multitarget mechanisms capable of rapidly inactivating pathogens while minimizing the likelihood of resistance development.[2-4]

Among emerging approaches, light-activated antimicrobial systems have attracted significant attention. These systems generate reactive oxygen species (ROS) directly at the site of illumination, enabling rapid and broad-spectrum eradication of bacteria, fungi, and viruses.[5-7] Because ROS indiscriminately oxidize essential cellular components, the resulting damage

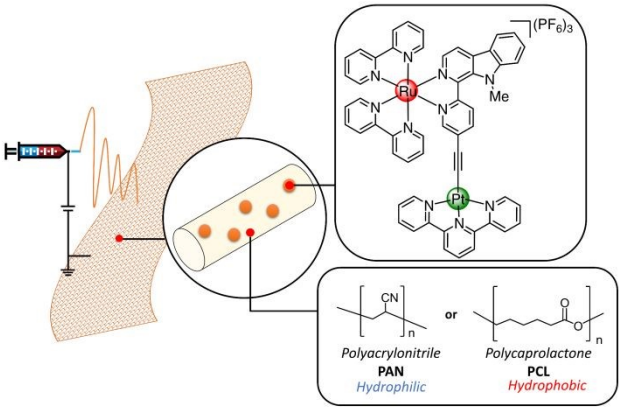

Fig. 1 Schematic illustration of formation of electrospun nanofibers doped with luminescent Ru-Pt complex in hydrophobic (PCL) and hydrophilic (PAN) matrices.

[a] Faculty of Chemistry, University of Duisburg-Essen, Universitätsstraße 5, Essen, 45141 Germany
[b] Department of Biophysics, Faculty of Medicine, Ruhr University Bochum, Universitätsstrasse 150, 44801 Bochum.
[c] Center for Protein Diagnostics (PRODI), Ruhr University Bochum, Gesundheitscampus 4, 44801 Bochum, Germany
[d] Center for Nanointegration Duisburg-Essen (CENIDE), Center of Medical Biotechnology (ZMB) and Center for Water and Environment Research (ZWU), Universitätsstraße 5, Essen, 45141 Germany, Email: anzhela.galstyan@uni-due.de
# These authors contributed equally to this work.

View Article Online
DOI: 10.1039/D6TB00671J

occurs through multiple simultaneous pathways, making microbial resistance highly unlikely.[8, 9]

This mechanism forms the basis of antimicrobial photodynamic therapy. During this process, a photosensitizer (PS) absorbs visible light and is promoted to an excited singlet state, followed by intersystem crossing to a long-lived triplet excited state. This excited state can interact with molecular oxygen through either energy transfer (Type II mechanism), producing singlet oxygen, or electron transfer reactions (Type I mechanism), generating radical ROS such as superoxide and hydroxyl radicals.[10] These highly reactive species rapidly oxidize cellular structures, leading to irreversible microbial inactivation.[11, 12] A wide range of organic and inorganic photosensitizer systems have been explored in this context, including porphyrinoids, phthalocyanines, xanthene dyes, and transition-metal complexes.[13-19] Among these systems, ruthenium-based complexes are particularly attractive due to their strong visible-light absorption, long-lived triplet excited states, and efficient ROS generation.[10, 20-25] Notably, the compound TLD-1433 has advanced into phase II clinical trails for bladder cancer.[16, 17] Studies have shown that the incorporation of a second heavy metal center, can further enhance photophysical performance by increasing spin–orbit coupling, improving photostability under repeated irradiation, and modulating redox properties that influence the balance between Type I and Type II ROS pathways.[26-31]

To enable practical and effective applications beyond solution-phase studies, PSs are increasingly being incorporated into functional materials.[32-35] Immobilization of the photosensitizers into polymer matrices, hydrogels, nanocomposites, or thin films enables their integration into coatings, membranes, or medical devices designed for continuous antimicrobial activity.[36-39] Such material platforms can improve photosensitizer stability, prevent leaching, and facilitate localized ROS generation at surfaces where microbial contamination occurs.[40] Despite substantial progress, many photoactive materials still suffer from limitations such as restricted oxygen transport and insufficient surface area for efficient light harvesting and ROS diffusion. Electrospun nanofibrous materials provide an effective strategy to overcome these challenges. Electrospinning enables the fabrication of membranes composed of ultrafine fibers with extremely high specific surface area, interconnected porosity, and tunable nanoscale morphology.[41-43] These structural characteristics enhance photon absorption, facilitate oxygen diffusion throughout the material, and allow rapid transport of generated ROS to microbial targets. Polyacrylonitrile (PAN) is widely used for electrospinning due to its excellent fiber-forming ability, chemical resistance, and mechanical robustness. The presence of polar nitrile groups promotes strong intermolecular interactions, enabling the formation of mechanically stable nanofibrous membranes with high surface area and controlled porosity. Poly(ε-caprolactone) (PCL) is widely employed as a polymer matrix owing to its biocompatibility, biodegradability, and mechanical flexibility. As a semi-crystalline aliphatic polyester, PCL undergoes slow hydrolytic degradation under physiological conditions, making it attractive for biomedical surfaces and antimicrobial interfaces.

In this study, the chemical synthesis, photophysical and biological evaluation of the encapsulation of a binuclear ruthenium-platinum photosensitizer into electrospun nanofibrous membranes for antimicrobial photodynamic therapy is reported. While traditional ruthenium complexes interact by energy transfer to molecular oxygen in order to generate singlet oxygen, [44, 45] the binuclear ruthenium-platinum complex was found to be capable of producing singlet oxygen by energy transfer as well as superoxide by electron transfer, presenting a photosensitizer that can interact by combined type I and type II mechanisms.[46] This dual reactivity provides mechanistic flexibility and may enhance antimicrobial performance under conditions where oxygen availability is limited. Furthermore, the presence of the platinum center increases spin–orbit coupling, promoting efficient intersystem crossing and enhancing triplet-state reactivity, while also enabling modulation of redox properties and reactive oxygen species selectivity. Using electrospinning techniques, the metal complex was incorporated into PAN and PCL membranes and the respective biomaterials produced (Fig. 1). The respective membranes were found with homogeneous photosensitizer distribution and stable fiber morphology. Comparative evaluation of the polymer matrices further showed that polymer physicochemical properties strongly influence photosensitizer retention, fouling behavior, and overall operational stability. While both membrane systems displayed pronounced light-activated antibacterial activity, the PAN-based membranes demonstrated greater structural robustness and maintained their efficacy during repeated biological exposure. Under visible-light irradiation, both membrane systems exhibited strong antibacterial activity against Gram-positive and Gram-negative bacteria.

Results and discussion

Synthesis and photophysical characterization of Ru-Pt complex

The heterobimetallic RuPt dyad, described in a previous work of the group, was constructed via a modular synthetic strategy that enables the stepwise assembly of the organic scaffold and subsequent metal coordination.[47] The ligand framework was first established through condensation and oxidative aromatization, followed by N-methylation to modulate the electronic properties of the heteroaromatic core. Installation of a protected ethynyl linker by Sonogashira coupling provided a versatile handle for further functionalization. Coordination to the Ru(II) center was then achieved under hydrothermal conditions, affording a stable $Ru(bipy)_2$-based complex. Subsequent deprotection of the terminal alkyne enabled the final coupling step with a terpyridine-coordinated Pt(II) fragment, yielding the targeted RuPt heterobimetallic architecture (Fig. 2 and Fig. S1-S24). This convergent approach allows precise control over the spatial arrangement of the two metal centers, facilitating electronic communication between the Ru photosensitizer and the Pt catalytic site.[47] RuPt remained stable under physiological conditions and light irradiation (Fig. S32-33).

View Article Online
DOI: 10.1039/D6TB00671J

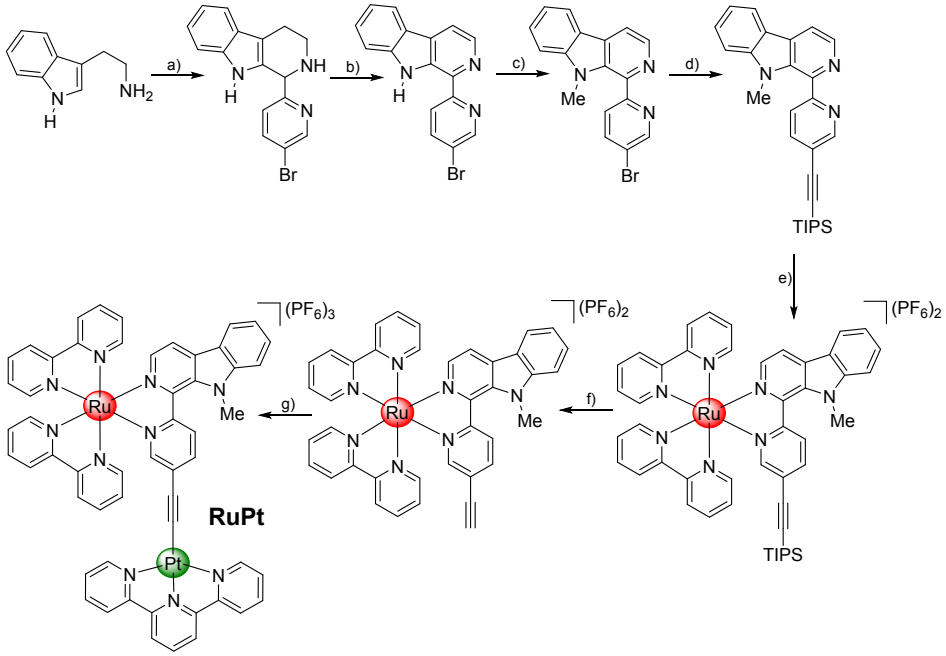

Fig. 2. Synthesis of RuPt investigated in this study. Conditions and reagents: a) 5-bromo-2-pyridinecarboxaldehyde, anisole, reflux, 3 h; b) MnO_2, reflux, 21 h. c) NaH, MeI, DMF, 0 °C → rt, overnight; d) (triisopropylsilyl)acetylene, $Pd(PPh_3)_4$, NEt_3, CuI, DMF, 65 °C, overnight; e) $Ru(bipy)_2Cl_2$, EtOH:H_2O (1:1), pressure flask (120 °C), 24 h; f) TBAF, AcOH, ACN:THF (2:1), rt, overnight; g) [Pt(terpy)Cl]Cl, CuI, NEt_3, DMF, rt, 72 h.

Table 1. Photophysical properties of RuPt solutions in H_2O:DMSO (99:1, v:v). λ_{abs} = absorption maximum; λ_{em} = emission maximum; τ = photoluminescence lifetime; Φ_{PL} = photoluminescence quantum yield; Φ_{Δ} = singlet oxygen quantum yield. Table adapted from our previous work.[47]

Complex	λ_{abs}/nm (ε/M-1cm-1)	λ_{em}/nm	τ/ns (contribution/%)	Φ_{PL}/%	Φ_{Δ}/%
RuPt	286 (64650), 325 (44367), 428 (25311), 482 (10918)	676	8 (24) 311 (76)	1	88

indicating sufficient

RuPt exhibits multiple absorption bands across the UV and visible spectra (Fig. S27). The intense high-energy bands at 286 and 325 nm correspond to ligand-centered (LC) π→π* transitions, while the lower-energy bands at 428 and 482 nm lie in the visible region and are characteristic of metal-to-ligand charge transfer (MLCT) transitions, primarily involving ruthenium orbitals and the π* orbitals of the coordinated ligands. The significant absorption extending to 482 nm demonstrates efficient visible-light harvesting, an important feature for photocatalytic and photosensitizing applications. The moderate molar absorptivity at 482 nm indicates partial mixing of MLCT states with other electronic configurations, likely influenced by the attached platinum fragment, which may modulate the complex's photophysical behavior. Upon photoexcitation, RuPt exhibits a broad emission band centred at 676 nm, located in the red region of the spectrum. This emission is typical of a triplet MLCT (^{3}MLCT) excited state in ruthenium polypyridyl complexes. The significant Stokes shift between the lowest-energy absorption band (482 nm) and the emission maximum (676 nm) reflects substantial excited-state structural relaxation and charge redistribution. Such behaviour is consistent with population of a relaxed ^{3}MLCT state prior to radiative decay as previously described for ruthenium polypyridine complexes.[48-50] Time-resolved emission measurements reveal biexponential decay with lifetimes of 8 ns (24%) and 311 ns (76%). The dominant long-lived component indicates that emission primarily originates from a stabilized triplet excited state. The minor short-lived component may arise from conformational heterogeneity, partial excited-state quenching, or weak electronic communication between the ruthenium and platinum centres that introduces additional non-radiative pathways. The lifetime distribution suggests the presence of closely spaced triplet states or multiple deactivation channels within the excited-state manifold. Despite the relatively long-lived triplet state, the photoluminescence quantum yield (Φ_{PL}) is low (1%), indicating that radiative decay is strongly outcompeted by non-radiative processes. Notably, RuPt exhibits an exceptionally high singlet oxygen quantum yield (Φ_{Δ} = 88%), demonstrating highly efficient triplet–triplet energy transfer to ground-state molecular oxygen. The combination of suppressed emission and near-quantitative $^1O_2$ generation is consistent with enhanced spin–orbit coupling induced by the heavy platinum centre. Overall, RuPt retains the characteristic MLCT photophysical signature of ruthenium polypyridyl complexes while displaying markedly enhanced triplet-state reactivity. For direct comparison, singlet oxygen generation was quantified also by time-resolved detection of the characteristic $^1O_2$ phosphorescence at 1270 nm for both RuPt and

View Article Online
DOI: 10.1039/D4TB00671J

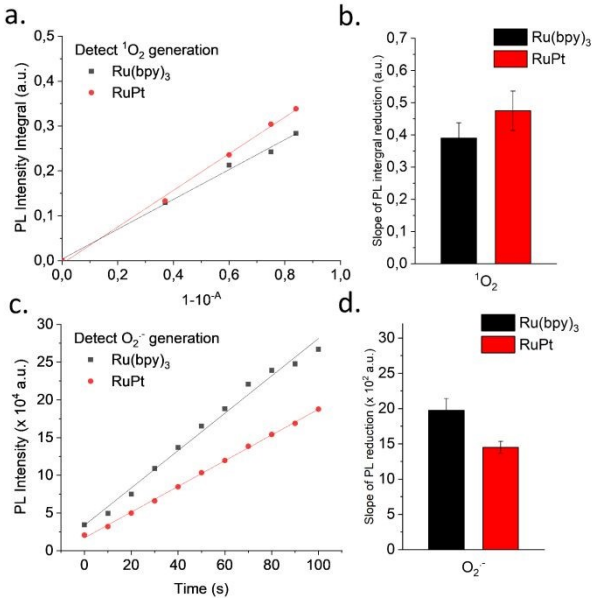

Fig.3. Comparison of reactive oxygen species (ROS) generation by $Ru(bpy)_3$ and RuPt. (a) Representative Stern–Volmer plots of photoluminescence (PL) intensity integral for singlet oxygen ($^1O_2$) detection. (b) Mean slopes of the PL integral decay derived from independent experimental replicates, shown with standard deviations. (c) Representative time-dependent PL intensity of DHE used for superoxide ($O_2^{\bullet-}$) detection. (d) Mean slopes of the PL intensity increase obtained from independent measurements, shown with the corresponding standard deviations.

$[Ru(bpy)_3]^{2+}$ (Fig. S29 and S30). In parallel, superoxide radical formation was evaluated using dihydroethidium (DHE) as a chemical probe (Fig. S31). These comparative measurements allow direct assessment of the influence of the Pt fragment on reactive oxygen species generation relative to the parent $Ru(bpy)_3^{2+}$ chromophore (Fig. 3).

The parent $Ru(bpy)_3^{2+}$ complex exhibits a long-lived triplet metal-to-ligand charge transfer (^{3}MLCT) excited state that is capable of both photochemical pathways. In solution, $Ru(bpy)_3^{2+}$ has measurable $^1O_2$ quantum yields, though lower than many archetypal Type II photosensitizers. For example, reported Φ_Δ values of $Ru(bpy)_3^{2+}$ vary with solvent (e.g., moderate values in acetonitrile/methanol and lower in aqueous media), indicating incomplete energy-transfer efficiency to molecular oxygen. The data presented in Fig. 3 a–d compare the ROS generation efficiency of RuPt and $Ru(bpy)_3$, evaluated via direct measurement of photoluminescence (PL) emission at 1270 nm for $^1O_2$ and PL probe responses for superoxide ($O_2^{\bullet-}$). The integrated PL intensity exhibits a linear dependence on ($1 - 10^{-A}$), confirming that changes in emission scale proportionally with photoinduced $^1O_2$ production. Notably, RuPt shows a steeper slope than $Ru(bpy)_3$, indicating more efficient $^1O_2$ formation. This enhancement suggests that incorporation of Pt into the Ru-based framework facilitates intersystem crossing and increases triplet-state population, thereby promoting energy transfer to molecular oxygen. In contrast, panels (c) and (d) reveal that $Ru(bpy)_3$ generates superoxide more efficiently than RuPt. The time-dependent PL response shows a significantly steeper slope for $Ru(bpy)_3$ compared to RuPt, indicating a stronger propensity for electron-transfer processes leading to $O_2^{\bullet-}$ formation, characteristic of a Type I photoreaction pathway. This shift in photochemical behaviour suggests that RuPt modulates ROS selectivity rather than simply enhancing overall ROS production. Nevertheless, RuPt still produces substantial amounts of $O_2^{\bullet-}$, consistent with a combined Type I and Type II photochemical profile.

Nanofabrication

Composite nanofibrous membranes (NFMs) incorporating the Ru–Pt complex were fabricated under optimized electrospinning conditions to obtain uniform, bead-free fibers with homogeneous PS distribution (see ESI for full experimental details). The polymer solution composition, viscosity, applied voltage, flow rate, and tip-to-collector distance were systematically adjusted to ensure stable jet formation and prevent phase separation of the metal complex during fiber formation. The PAN-RuPt solution contained 10 wt% polymer dissolved in pure DMF, whereas the PCL-RuPt spinning solution consisted of 15 wt% polymer dissolved in a tetrahydrofuran/dimethylformamide (THF/DMF) solvent mixture (1:1 v/v). Electrospinning was performed under optimized operating conditions for each formulation. PAN-RuPt fibers were produced at a flow rate of 3.00 mL h^{-1} using an applied voltage of 25 kV and a TCD of 10 cm. In contrast, The PCL-RuPt solution was processed at a flow rate of 1.20 mL h^{-1} and an applied voltage of 20 kV with a tip-to-collector distance (TCD) of 15 cm. These parameter adjustments enabled stable fiber formation and uniform morphology for both polymer systems. Fig. 4 shows scanning electron microscopy (SEM) images and fiber diameter distribution of PAN-RuPt and PCL-RuPt Fiber diameter analysis was performed using ImageJ software, with measurements collected from more than 100 randomly selected locations, ensuring statistically relevant evaluation of the fiber morphology. (Fig. S25). The PAN-based membranes exhibit a regular and narrow fiber diameter distribution, with an average diameter of 0.64 ± 0.10 μm. In contrast, the PCL-based membranes show pronounced irregularities, such as thickened, nonuniform, and fused fibers, with an average diameter of 1.16 ± 0.69 μm. Some regions exhibit uneven distribution and local fiber adhesion, reflecting lower structural uniformity than the PAN-based membranes. Energy-Dispersive X-ray Spectroscopy (EDS) analysis confirmed successful incorporation of RuPt into membranes (Fig. S36 and S37).

View Article Online
DOI: 10.1039/D6TB00671J

ARTICLE

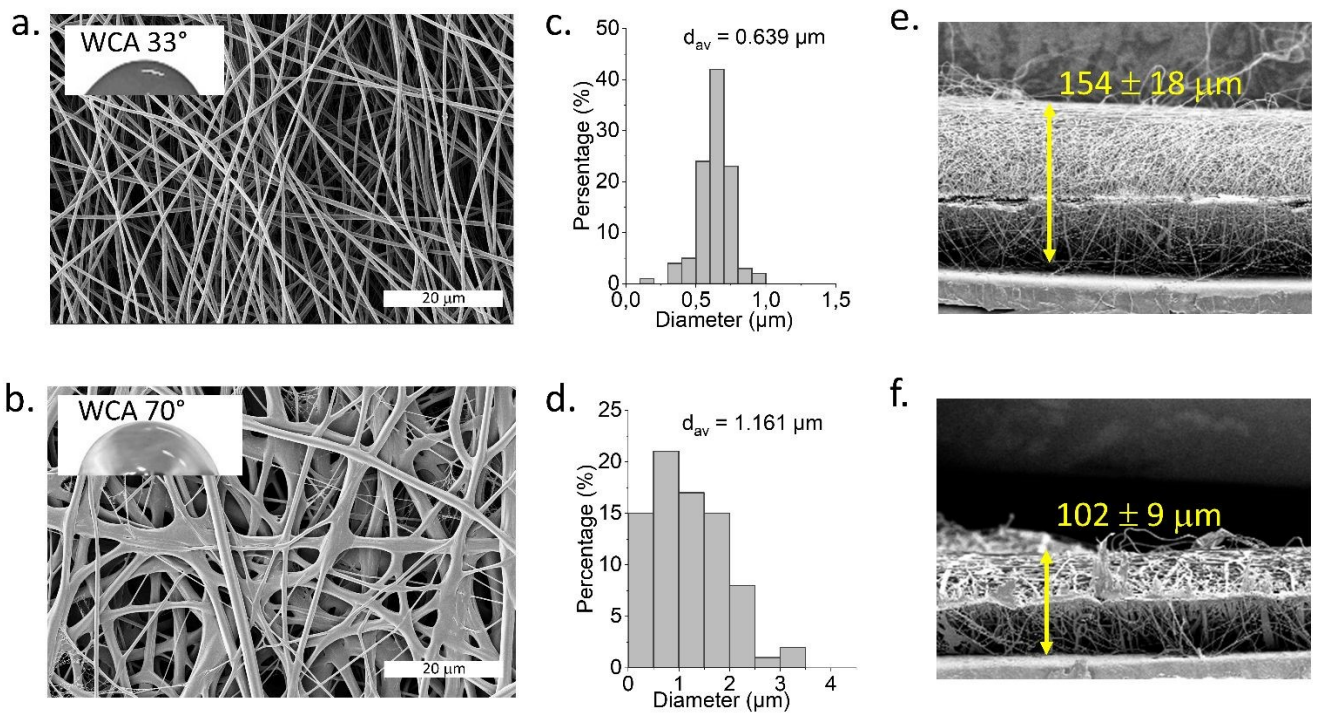

Fig. 4. SEM surface images of the membranes showing randomly oriented fiber networks with water contact angles (WCA) of 33° for PAN-RuPt (a) and 70° for PCL-RuPt (b), respectively (insets: corresponding water droplet images). (c, d) Fiber diameter distributions of the membranes in (a) and (b). Fiber diameter analysis was performed using ImageJ software, with measurements collected from more than 100 randomly selected locations, ensuring statistically relevant evaluation of the fiber morphology. (e, f) Cross-sectional SEM images showing the membrane thicknesses, with the reported values representing the average of more than 30 measurements, including the corresponding standard deviation.

The surface wettability of the NFMs was assessed by water contact angle (WCA) measurements. As anticipated, the PAN-based NFM exhibited hydrophilic behavior, characterized by a WCA of 33°, whereas the PCL-based NFM displayed hydrophobic properties, with a higher WCA of 70° (Fig.4 and Fig. S26).

The photoinduced antibacterial activity of the obtained materials relies on their ability to absorb visible light, which is directly related to the amount of PS incorporated into the nanofibers. The PS loading in the nanofiber membranes was quantified by UV–Vis spectroscopy after complete dissolution of a certain amount of membranes in DMF (Fig. S34). The PAN–RuPt membrane exhibited a PS loading of ca. 2.24 wt% with a loading efficiency of 50.10 ± 4.70 %, whereas the PCL–RuPt membrane showed a slightly lower loading of ca. 2.18 wt% and an efficiency of 45.20 ± 5,80 %. UV–vis diffuse reflectance spectroscopy was employed to analyze the surface chemical composition of the NFMs. As shown in Fig. 5a and 5b, the as-electrospun membranes (denoted as *n*) exhibit enhanced light absorption in the visible region. To evaluate the retention capability of the polymer matrix toward the PS, the membranes were washed with 70% ethanol and their absorption spectra were measured again (denoted as *w*). Finally, the washed membranes were irradiated for 1h, and the absorption spectra were recorded once more (denoted as *ir*). A clear difference in PS retention was observed between the two polymer matrices. For comparison, the absorption spectrum of the isolated RuPt complex (Fig. S28) exhibits characteristic MLCT bands in the same spectral region, confirming that the observed reflectance features of the membranes originate from the incorporated PS and remain largely preserved upon immobilization. The absorbance values shown in Fig. 5c and 5d were extracted at λ = 482 nm, corresponding to the main MLCT absorption maximum of the RuPt complex. As shown in Fig. 5, the PAN-based membranes exhibited excellent stability, with less than 10% loss of absorption intensity after both washing and irradiation. In contrast, the PCL-based membranes showed a substantially higher loss, exceeding 70% under the same conditions. This pronounced difference indicates that PAN provides a more effective matrix for immobilizing the PS, likely due to stronger polymer–PS interactions and reduced leaching compared to PCL. The $LogP_{o/w}$ value of Ru–Pt was determined to be −0.51, indicating a predominantly hydrophilic character and preferential retention in aqueous environments (Fig. S35).

View Article Online
DOI: 10.1039/D5TB00674H

Accordingly, Ru–Pt exhibited a higher release from the hydrophobic PCL matrix compared to PAN. This behavior can be attributed to the limited affinity of the hydrophilic complex toward the hydrophobic PCL network, facilitating its diffusion into the aqueous medium, whereas stronger interactions with the more polar PAN matrix may restrict its release.

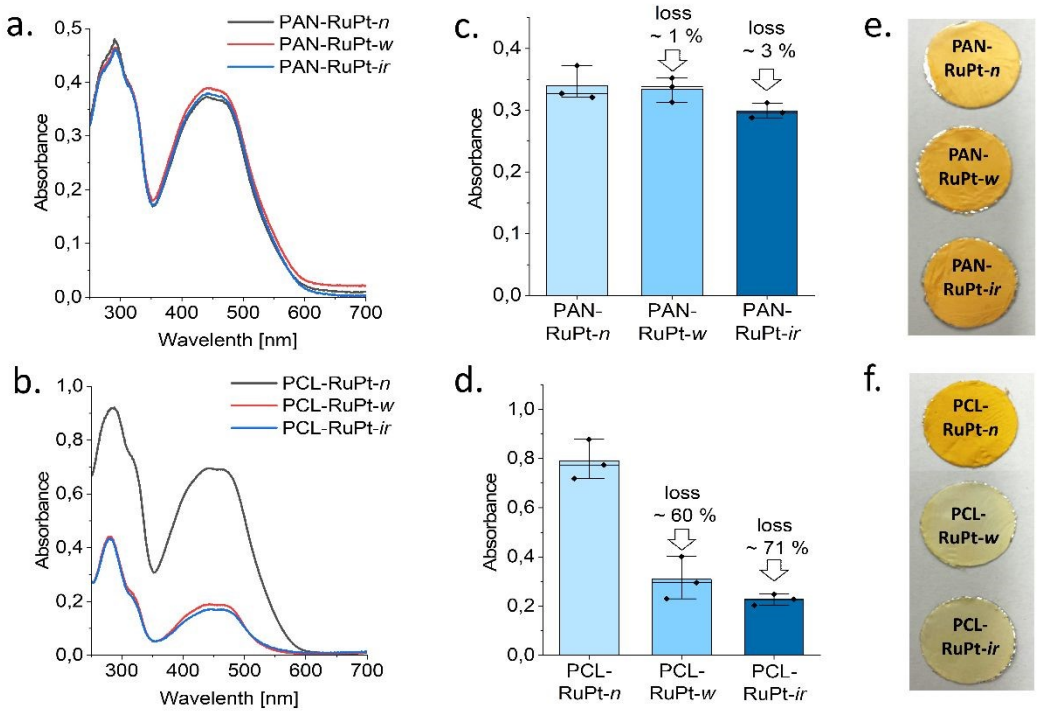

Fig. 5. UV–Vis reflectance absorbance spectra of (a) PAN–RuPt and (b) PCL–RuPt membranes in the pristine (n), washed (w), and irradiated (ir) states. (c,d) Corresponding absorbance values at the main absorption maximum for PAN–RuPt (c) and PCL–RuPt (d), showing the relative loss in absorbance after washing and irradiation (percentage losses indicated; mean ± SD, n = 3). Absorbance values were evaluated at 482 nm. Photographs of PAN–RuPt (e) and PCL–RuPt (f) membrane discs after the different treatments, revealing visible colour changes consistent with the spectroscopic data.

Biocompatibility

In nanostructured material design for antibacterial applications, a primary challenge is engineering a structural platform that achieves minimal toxicity against mammalian cells. The biocompatibility of NFMs was assessed toward the healthy fibroblast cell line GM-5657. Although the previously described Ru-Pt photosensitizer exhibited measurable dark toxicity (IC_{50} = 41.68 ± 3.27 µM) toward GM-5657 cells,[47] incorporation into the PAN and PCL membranes resulted in a favourable biocompatibility profile under the tested conditions (Fig. S38). Both RuPt-PAN and RuPt-PCL membranes maintained high cell viability, suggesting that immobilization within the polymer scaffolds reduces direct cellular exposure to cytotoxic concentrations of the free complex.

Photobiological evaluation

Bacillus subtilis (*B. subtilis,* Gram-positive) and *Escherichia coli* (*E. coli*, Gram-negative) were selected as representative model microorganisms to assess the broad-spectrum antimicrobial performance of the NFMs. Bacterial suspensions (10^6–10^7 CFU mL^{-1}) were incubated with the NFMs for 15 min and subsequently irradiated with broad-band LED light for 1 h (see ESI† for details). As shown in Fig. 6a and 6b in the absence of illumination, no statistically significant bacterial inactivation was observed for any of the membranes, confirming that dark toxicity is negligible. In contrast, light exposure resulted in dramatic decreases in viable bacteria. For *B. subtilis*, irradiation of both PAN-RuPt and PCL-RuPt membranes produced reductions exceeding >3log_{10} unit (>99,9 % reduction). Against *E. coli*, light activation also significantly enhanced antibacterial performance, yielding reductions greater than 1 log_{10} unit (90% reduction) compared to dark controls. These findings underscore the essential role of light in activating the photodynamic process. The antibacterial activity is attributed to efficient ROS generation upon irradiation and their rapid diffusion from the NFM surface, which sustains high localized oxidative stress at the bacteria–membrane interface. Notably, the PCL-based membranes exhibited antibacterial efficacy comparable to PAN-based systems under identical irradiation conditions, despite containing a lower PS loading after sterilization/washing with 70% ethanol (Fig. 6b and 6d). This effect may be attributed to enhanced bacterial interaction with the more hydrophobic PCL surface, promoting closer cell–material contact. Such proximity would reduce the effective diffusion distance required for short-lived ROS species, thereby compensating for the lower PS content and enabling efficient photodynamic inactivation. The greater susceptibility of *B. subtilis* relative to *E. coli* likely reflects structural differences in

View Article Online
DOI: 10.1039/D6TB00671J

cell envelope architecture. Gram-positive bacteria lack an outer membrane barrier, facilitating ROS diffusion and enhancing photodynamic damage. In contrast, the outer membrane of Gram-negative *E. coli* may partially restrict ROS penetration, resulting in comparatively reduced—but still substantial—bactericidal efficacy. Nevertheless, the viability reduction observed in *E. coli* demonstrates that the system overcomes key permeability barriers, a critical requirement for translational antimicrobial photodynamic platforms.

Live/dead imaging corroborates these findings at the cellular level. Control samples show predominantly green fluorescence (intact membranes), whereas irradiated RuPt-functionalized NFMs exhibit red staining, indicative of compromised membrane integrity. The marked increase in red fluorescence in *B. subtilis* following light exposure aligns with ROS-mediated membrane disruption as a primary bactericidal pathway.

Furthermore, sodium azide was utilized as a $^1O_2$ quencher, given its well-established role as a diagnostic probe in oxidative systems attributable to its high quenching rate constant for $^1O_2$.[51, 52] Under purely Type II photochemistry, azide would be expected to diminish oxidative stress by dissipating $^1O_2$. energy non-productively. However, our data indicate that bacterial killing is not attenuated in the presence of azide; rather, it is enhanced. This suggests that Type I photochemical processes dominate in this system or become favored in the presence of azide. The paradoxical potentiation observed here strongly argues against a $^1O_2$–exclusive mechanism of bacterial photoinactivation. Instead, the data are consistent with a redirection of excited-state photochemistry toward electron-transfer reactions. In this scenario, the excited PS interacts directly with azide anions, generating azidyl radicals (N_3•) through one-electron oxidation.[53, 54] These nitrogen-centered radicals possess strong oxidizing potential and are capable of initiating secondary radical cascades, including lipid peroxidation and protein side-chain oxidation. Notably, to the best of our knowledge, such azide-mediated potentiation of photodynamic activity has not previously been reported for transition-metal photosensitizers, highlighting a previously unrecognized pathway for modulating the photochemistry and antimicrobial activity of metal-based complexes. Unlike $^1O_2$ — which is characterized by a short lifetime and limited diffusion radius in aqueous environments—azidyl radicals may propagate damage beyond the immediate site of photosensitizer localization, thereby broadening the spectrum and magnitude of bactericidal effects.

Fig. 6. Light-activated antibacterial activity of Ru-functionalized polymers. CFU (log scale) of B. subtilis (a) and E. coli (b) after exposure to PAN–RuPt and PCL–RuPt under dark and light conditions ± NaN_3. CFU data represent mean ± SD (n = 3 independent experiments) Representative live/dead fluorescence images of *B. subtilis* (c) and *E. coli* (d). Green indicates viable cells and red indicates membrane-compromised/dead cells.

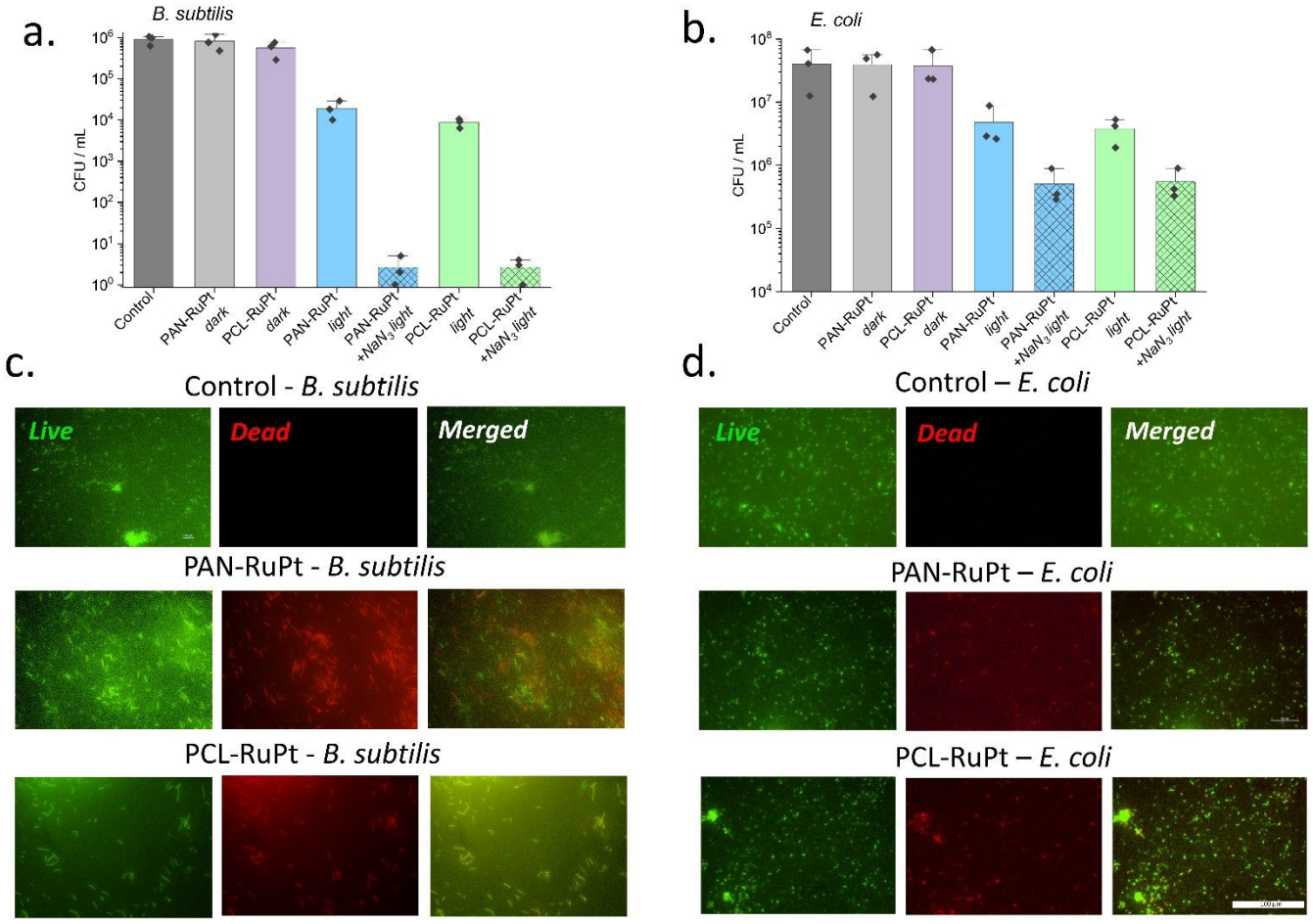

View Article Online
DOI: 10.1039/D6TB00671J

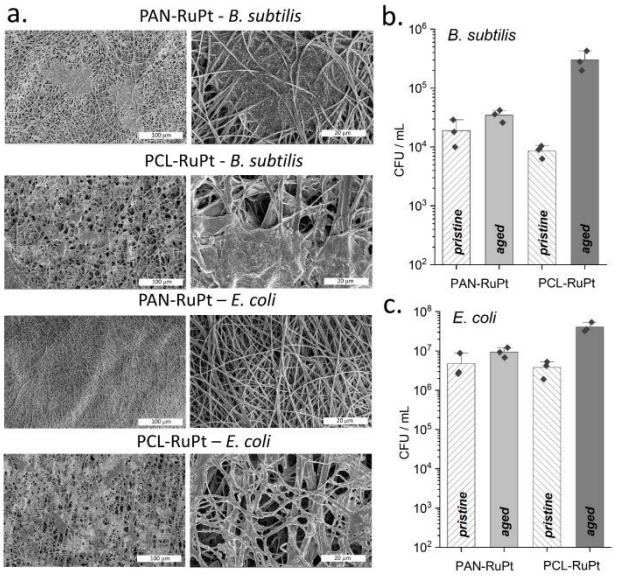

Fig. 7. a) Representative SEM images of PAN–RuPt and PCL–RuPt membranes after 3 days of incubation in B. subtilis or E. coli suspensions. Quantitative CFU analysis (log scale) of *B. subtilis* (b) and *E. coli* (c) after irradiation of pristine and aged membranes.

This shift toward radical-mediated toxicity may be particularly consequential in bacteria, where structural compartmentalization influences ROS accessibility. In Gram-negative organisms, the outer membrane restricts penetration of many oxidants, while in Gram-positive bacteria, the thick peptidoglycan layer imposes distinct diffusion constraints. A diffusible radical intermediate could partially overcome these barriers, amplifying membrane damage and facilitating intracellular oxidative injury. The enhanced killing observed in the presence of azide therefore likely reflects not merely additive oxidative stress but a qualitative change in the nature of the reactive species involved.

A notable implication is that, because $^1O_2$ generation strictly depends on molecular oxygen, classical Type II photochemistry is inherently oxygen-limited. In contrast, Type I pathways involving direct electron transfer can proceed with reduced oxygen dependence, relying instead on radical propagation chemistry. This distinction may be particularly relevant in biofilms or infected tissues characterized by steep oxygen gradients. The ability to maintain—or even enhance—bactericidal efficacy under such conditions represents a significant translational advantage. Moreover, bacterial antioxidant defenses, which are primarily optimized to detoxify superoxide, hydrogen peroxide, and organic peroxides, are unlikely to efficiently neutralize azidyl radicals. The absence of dedicated enzymatic scavenging systems for nitrogen-centered radicals may create a specific vulnerability, amplifying oxidative imbalance and overwhelming redox homeostasis. Collectively, these findings support a revised conceptual framework in which sodium azide acts not merely as a passive $^1O_2$ quencher, but as an active modulator of photochemical reactivity capable of reshaping bactericidal mechanisms.

Durability of NFMs

To compare the photoantibacterial performance and long-term structural stability of PAN- and PCL-based membranes, we evaluated membrane aging and biofouling under realistic operational conditions. Membranes were incubated in bacterial suspensions for 3 days to simulate prolonged exposure. No dark toxicity was observed. Following disinfection, the aged membranes were subjected to a second irradiation cycle under identical experimental parameters.

SEM characterization (Fig. 7a) demonstrates the development of a fouling layer on both materials after 3 days of incubation in bacterial suspensions. However, the extent and morphology of fouling differ markedly. PAN-based membranes retain a largely discernible fibrous architecture, with partial surface deposition but preserved pore structure. In contrast, PCL membranes exhibit extensive surface coverage, dense biofouling accumulation, and pronounced pore occlusion, indicating substantial structural compromise. These morphological differences directly correlate with functional performance. Quantitative CFU analysis (Fig. 7b and 7c) shows that aged PAN–RuPt membranes maintain antibacterial efficacy comparable to their pristine counterparts, with only modest increases in surviving bacterial counts for both *B. subtilis* and *E. coli*. Conversely, aged PCL–RuPt membranes display a pronounced reduction in antibacterial performance, evidenced by significantly elevated CFU levels relative to pristine samples.

The greater susceptibility of PCL to fouling likely arises from its intrinsic physicochemical properties. As a more hydrophobic and mechanically softer polymer, PCL may promote stronger bacterial adhesion and extracellular polymeric substance (EPS) accumulation, accelerating biofilm consolidation. Progressive pore blockage and surface masking can limit light penetration, reduce oxygen diffusion, and hinder ROS interaction with bacterial cells—thereby attenuating photodynamic efficiency during subsequent irradiation cycles. In contrast, PAN appears to better resist structural collapse and excessive biofilm accumulation, preserving active surface area and maintaining effective photoinduced antibacterial activity. In contrast, PCL is a biodegradable, hydrophobic polyester valued for its tunable mechanical properties and excellent electrospinning processability, particularly in filtration and biomedical contexts. PAN and PCL represent two contrasting classes of polymer substrates widely employed in membrane technologies, and their distinct physicochemical properties critically influence performance, fouling susceptibility, and operational lifetime.

Conclusions

In conclusion, the encapsulation of a binuclear ruthenium–platinum photosensitizer within electrospun nanofibrous membranes, yielding materials with high surface area, structural integrity, and robust photodynamic activity is reported. Unlike conventional mononuclear ruthenium complexes, which predominantly generate singlet oxygen by

energy transfer, the binuclear ruthenium–platinum system operates through dual photochemical pathways, producing both singlet oxygen and superoxide radicals. The photosensitizer was incorporated into electrospun membranes composed of PAN and PCL, producing high-surface-area nanofibers. Systematic optimization of the fabrication process yielded bead-free fibers with controlled morphology, while comparative analysis revealed enhanced photosensitizer retention and structural stability within the hydrophilic PAN matrix. Under visible-light irradiation, both membrane types demonstrated potent antibacterial activity against Gram-positive and Gram-negative bacteria. The addition of sodium azide enhanced bacterial inactivation, indicating a shift from predominantly singlet-oxygen–mediated damage to radical-driven oxidative stress. Durability assessments under prolonged bacterial exposure showed that membrane performance depends not only on molecular photochemistry but also on matrix-specific antifouling properties. PAN–RuPt membranes maintained structural integrity and antibacterial activity over time, whereas PCL-based membranes exhibited significant fouling and reduced efficacy. Both membranes do not exhibit significant cytotoxicity toward the healthy fibroblast cell line GM-5657. These findings establish a clear connection between photosensitizer molecular design, nanofiber fabrication strategies, and long-term functional performance, providing a framework for the development of next-generation photodynamic antimicrobial materials. Future studies may explore the translation of this approach to diverse biomedical and environmental applications, including wound dressings, surface coatings, and water treatment, where sustained antimicrobial performance under light activation is essential.

Conflicts of interest

There are no conflicts to declare.

Data availability

All data supporting the findings of this study are available within the article and its Electronic Supplementary Information (ESI).

Acknowledgements

This work was supported by the MERKUR foundation of Mercator Research Center Ruhr (Grant number Ko-2023-0009). A. Galstyan also acknowledges support from German Research Foundation (Grant number GA2362/6-1) and COST Action PanEuCOPT - Pan European Commission on Photoantimicrobial Testing (CA24127). J. Karges gratefully acknowledges the financial support provided by the Liebig fellowship from the Chemical Industry Fund of the German Chemical Industry Association, the Life Sciences Bridge Award from the Aventis Foundation, and the Paul Ehrlich & Ludwig Darmstaedter Early Career Award 2024 – a prize awarded by the Paul Ehrlich Foundation, Germany.

Notes and references

1. B. Aslam and S. F. Aljasir, *Antibiotics (Basel)*, 2025, **14**.
2. A. Frei, A. D. Verderosa, A. G. Elliott, J. Zuegg and M. A. T. Blaskovich, *Nature Reviews Chemistry*, 2023, **7**, 202-224.
3. T. W. Rees, P.-Y. Ho and J. Hess, *ChemBioChem*, 2023, **24**, e202200796.
4. S. M. Sebastian, D. Nag and A. Galstyan, *ACS Applied Materials & Interfaces*, 2026, **18**, 8867-8880.
5. D. García-Fresnadillo, *ChemPhotoChem*, 2018, **2**, 512-534.
6. L. Costa, M. A. Faustino, M. G. Neves, A. Cunha and A. Almeida, *Viruses*, 2012, **4**, 1034-1074.
7. H. Majiya, K. F. Chowdhury, N. J. Stonehouse and P. Millner, *Journal of Water Process Engineering*, 2019, **30**, 100475.
8. M. Wainwright, T. Maisch, S. Nonell, K. Plaetzer, A. Almeida, G. P. Tegos and M. R. Hamblin, *Lancet Infect. Dis.*, 2017, **17**, e49-e55.
9. M. Chittò, D. Tutschner, U. Dobrindt, A. Galstyan and M. Berger, *Communications Biology*, 2025, **8**, 1413.
10. C. Mari, V. Pierroz, S. Ferrari and G. Gasser, *Chemical Science*, 2015, **6**, 2660-2686.
11. R. Tanu, A. A. Chaudhary, G. Prakash, N. Yasmeen, M. A. M. Ali, N. Raza, P. K. Sharma, A. Kumar, T. Yadav and V. Kumar, *Frontiers in Cellular and Infection Microbiology*, 2025, **Volume 15 - 2025**.
12. A. Sowa, A. Höing, U. Dobrindt, S. K. Knauer, A. Galstyan and J. Voskuhl, *Chem. Eur. J.*, 2021, **27**, 14672-14680.
13. C. Spagnul, L. C. Turner and R. W. Boyle, *Journal of Photochemistry and Photobiology B: Biology*, 2015, **150**, 11-30.
14. A. C. Mendes, N. M. M. Moura, M. A. F. Faustino, M. G. P. M. S. Neves and I. S. Chronakis, *BBA Advances*, 2025, **7**, 100160.
15. S. M. Stepping, N. Vashistha, S. Ullah, P. Liu, M. Anjass and B. Dietzek-Ivanšić, *RSC Advances*, 2024, **14**, 32501-32505.
16. S. A. McFarland, A. Mandel, R. Dumoulin-White and G. Gasser, *Current Opinion in Chemical Biology*, 2020, **56**, 23-27.
17. S. Monro, K. L. Colón, H. Yin, J. Roque, III, P. Konda, S. Gujar, R. P. Thummel, L. Lilge, C. G. Cameron and S. A. McFarland, *Chemical Reviews*, 2019, **119**, 797-828.
18. A. Galstyan, A. R. Naziruddin, C. Cebrián, A. Iordache, C. G. Daniliuc, L. De Cola and C. A. Strassert, *Eur. J. Inorg. Chem.*, 2015, **2015**, 5822-5831.
19. A. Galstyan, *Chem. Eur. J.*, 2021, **27**, 1903-1920.
20. L. K. McKenzie, H. E. Bryant and J. A. Weinstein, *Coordination Chemistry Reviews*, 2019, **379**, 2-29.
21. S. Bonnet, *Journal of the American Chemical Society*, 2023, **145**, 23397-23415.
22. Y. Husiev, S. K. Götzfried, M. L. A. Hakkennes, D. Kotova, I. Tutein Nolthenius, C. van de Griend, A. C. Johns, S. Abyar, M. A. Siegler, A. Kornienko and S. Bonnet, *Journal of the American Chemical Society*, 2025, **147**, 44356-44371.
23. J. Karges, *Angewandte Chemie International Edition*, 2022, **61**, e202112236.
24. D. Havrylyuk, A. C. Hachey, A. Fenton, D. K. Heidary and E. C. Glazer, *Nature Communications*, 2022, **13**, 3636.
25. L. Zeng, P. Gupta, Y. Chen, E. Wang, L. Ji, H. Chao and Z.-S. Chen, *Chemical Society Reviews*, 2017, **46**, 5771-5804.
26. S. Swavey and K. J. Brewer, *Inorganic Chemistry*, 2002, **41**, 6196-6198.
27. A. A. Holder, S. Swavey and K. J. Brewer, *Inorganic Chemistry*, 2004, **43**, 303-308.
28. A. A. Holder, D. F. Zigler, M. T. Tarrago-Trani, B. Storrie and K. J. Brewer, *Inorganic Chemistry*, 2007, **46**, 4760-4762.

29. M. Shee, J. Schleisiek, N. Maity, G. Das, N. Montesdeoca, M.-H. Ha-Thi, K. R. Gore, J. Karges and N. D. P. Singh, *Small*, 2025, **21**, 2408437.
30. P. Siekierski, E. Michaltsis, J. Schleisiek, N. Montesdeoca and J. Karges, *Chemical Communications*, 2025, **61**, 17424-17427.
31. N. Montesdeoca, Z. Papadopoulos, H. M. Tran, S. K. Hinojosa, H. Sielhorst, J. Heinen-Weiler and J. Karges, *Journal of the American Chemical Society*, 2026, **148**, 15640-15654.
32. K. Socha, I. Gusev, P. Mroczko and A. Blacha-Grzechnik, *RSC Advances*, 2025, **15**, 7905-7925.
33. N. Maldonado-Carmona, T.-S. Ouk, M. J. F. Calvete, M. M. Pereira, N. Villandier and S. Leroy-Lhez, *Photochemical & Photobiological Sciences*, 2020, **19**, 445-461.
34. Y. Gao, H. Lin, Y. Luo, J. Li, C. Gong, H. Chen and R. Gong, *Frontiers in Materials*, 2023, **Volume 10 - 2023**.
35. M. Vadala, D. C. Lupascu and A. Galstyan, *Photochemical & Photobiological Sciences*, 2024, **23**, 803-814.
36. A. Galstyan, H. Majiya and U. Dobrindt, *Nanoscale Adv.*, 2022, **4**, 200-210.
37. K. Strokov and A. Galstyan, *Eur. J. Org. Chem.*, 2020, **2020**, 7327-7332.
38. K. Strokov, A. H. Schäfer, U. Dobrindt and A. Galstyan, *ACS Appl. Bio Mater.*, 2020, **3**, 3751-3760.
39. F. Terlau, H. M. Martin and A. Galstyan, *Angew. Chem. Int. Ed.*, 2024, **63**, e202414412.
40. M. Q. Mesquita, C. J. Dias, M. G. P. M. S. Neves, A. Almeida and M. A. F. Faustino, *Molecules*, 2018, **23**, 2424.
41. A. Eldem, Y. Tekintaş, M. Ucuncu and N. Horzum, *Macromolecular Materials and Engineering*, 2025, **310**, 2500014.
42. C. Wang, Y. Su and J. Xie, *Accounts of Materials Research*, 2024, DOI: 10.1021/accountsmr.4c00145.
43. G. Wang, Z. Xu, Y. Qi, Y. Fang, G. Ning and J. Ye, *Chinese Chemical Letters*, 2024, **35**, 109503.
44. R. Youf, A. Nasir, M. Müller, F. Thétiot, T. Haute, R. Ghanem, U. Jonas, H. Schönherr, G. Lemercier, T. Montier and T. Le Gall, *Pharmaceutics*, 2022, **14**.
45. A. A. Mandal, A. Upadhyay, A. Mandal, M. Nayak, M. S. K, S. Mukherjee and S. Banerjee, *ACS Applied Materials & Interfaces*, 2024, **16**, 28118-28133.
46. L.-Y. Liu, J. Li, P. Sun, W. Yu, T.-Z. Ma, Y.-L. Zeng, Z. Zhao, Q. Wei, Y. Liu, J. P. Li, Z.-W. Mao and Z. Guo, *Journal of Medicinal Chemistry*, 2026, **69**, 4629-4641.
47. J. Sanz-Villafruela, L.-M. Servos, N. Montesdeoca, J. V. Cuevas-Vicario, A. J. Moro, J. C. Lima, M. Martínez-Alonso, G. Espino and J. Karges, *Inorganic Chemistry Frontiers*, 2025, DOI: 10.1039/D5QI00924C.
48. M. J. Cook, A. P. Lewis, G. S. G. McAuliffe, V. Skarda, A. J. Thomson, J. L. Glasper and D. J. Robbins, *Journal of the Chemical Society, Perkin Transactions 2*, 1984, DOI: 10.1039/P29840001293, 1293-1301.
49. A. Fennes, N. Montesdeoca, Z. Papadopoulos and J. Karges, *Chemical Communications*, 2024, **60**, 10724-10727.
50. V. Balzani and A. Juris, *Coordination Chemistry Reviews*, 2001, **211**, 97-115.
51. S. Cui, X. Guo, S. Wang, Z. Wei, D. Huang, X. Zhang, T. C. Zhu and Z. Huang, *Pharmaceuticals (Basel)*, 2024, **17**.
52. R. D. Hall and C. F. Chignell, *Photochemistry and Photobiology*, 1987, **45**, 459-464.
53. M. R. Hamblin, *Expert Review of Anti-infective Therapy*, 2017, **15**, 1059-1069. View Article Online DOI: 10.1039/D6TB00671J
54. L. Huang, T. G. St. Denis, Y. Xuan, Y.-Y. Huang, M. Tanaka, A. Zadlo, T. Sarna and M. R. Hamblin, *Free Radical Biology and Medicine*, 2012, **53**, 2062-2071.

View Article Online
DOI: 10.1039/D6TB00671J

All data supporting the findings of this study are available within the article and its Electronic Supplementary Information (ESI).